




Temperature-controlled nanomosaics of AuCu bimetallic structure towards smart light management

Wiktoria Lipińska^{1,*} , Katarzyna Grochowska¹, Jakub Karczewski^{2,3}, Jacek Ryl^{2,3}, and Katarzyna Siuzdak¹

¹Centre for Plasma and Laser Engineering, The Szewalski Institute of Fluid-Flow Machinery Polish Academy of Sciences, Fiszerza 14 St., 80-231 Gdańsk, Poland

²Institute of Nanotechnology and Materials Engineering, Faculty of Applied Physics and Mathematics, Gdańsk University of Technology, Narutowicza 11/12 St., 80-233 Gdańsk, Poland

³Advanced Materials Center, Gdańsk University of Technology, Narutowicza 11/12 St., 80-233 Gdańsk, Poland

Received: 19 February 2022

Accepted: 13 July 2022

© The Author(s) 2022

ABSTRACT

Gold–copper nanostructures are promising in solar-driven processes because of their optical, photocatalytic and photoelectrochemical properties, especially those which result from the synergy between the two metals. Increasing interest in their internal structure, such as the composition or distribution of the Au and Cu as well as the size and shape of the nanoparticles, have developed to define their physicochemical properties.

In this work, we present the influence of thermal treatment in temperature ranges from 100 to 600 °C on the formation process of bimetallic AuCu structures and their properties. AuCu materials were placed on nanostructured titanium foil substrates that were fabricated using electrochemical anodisation and chemical etching. Thin layers of AuCu mixture, as well as Au and Cu, were sputtered on the obtained Ti nanodimples. The materials were then annealed in a rapid thermal annealing furnace in an air atmosphere. Thermal treatment strongly affected the morphology and optical properties of the fabricated materials. AuCu NPs formed at 400 °C in titanium dimples. The material exhibits absorption of visible light in the range from c.a. 400 to 700 nm. The characterisation of the chemical nature of the samples was determined using X-ray photoelectron spectroscopy. In addition, X-ray diffraction and Raman spectroscopy defined composition and crystallinity. Based on photoelectrochemical studies carried out with the use of linear voltammetry in 0.1 M NaOH, it is possible to distinguish two types of interactions of light with the materials such as photogenerated charge accumulation and electron–hole pair separation. A 10AuCu electrode annealed at 300 °C achieved the highest current registered under illumination at – 0.17 V vs. Ag/AgCl/0.1 M KCl. The value was 11 times higher than for a non-annealed structure.

Address correspondence to E-mail: wlipinska@imp.gda.pl

<https://doi.org/10.1007/s10854-022-08775-9>

Published online: 06 August 2022

1 Introduction

Nowadays, a lot of effort has been directed to the control of the fine morphology of materials such as their size, shape, and homogeneity since at the nanoscale, the quantum confinement effect determines the overall performance. However, not only the material appearance but also its internal structure is of high importance and can make it suitable for a multitude of applications e.g. in catalytic reactions, photo-induced processes or the formation of hydrophobic surfaces [1]. The ability to control the properties of a nanomaterial and perform a comprehensive analysis are critically important tools in a scientist's hands in order to find applications in novel, highly efficient solar cells, water splitting devices, fuel cells, batteries, pollutant degradation devices, and sensors. Metals of dimensions limited by several or tens of nanometers are considered to be a very interesting objects due to a variety of unique properties such as electrical conductivity, catalytic, and optical activity [2] which are completely different from their bulk counterparts. Following that, research was focussed on pure metal nanoparticles (NPs) formed by noble metals (Au, Pt) [3, 4] and non-noble ones, typically in the form of oxides (Fe_2O_3 , TiO_2) [5, 6]. Next, combinations of both noble and non-noble element were proposed [7] and it was found that the chemical and physical properties of such structures were atypical compared to their pure elements, this being caused by the so-called synergetic effect. Among others, AuCu bimetallic structures have been extensively explored, where gold ensures higher resistance to the oxidation process than Cu, while copper oxide is a popular semiconducting oxide for photocatalytic applications [8]. As can be expected, various shapes of colloidal AuCu forms can be obtained, namely nanostars [9], nanocubes [10], and nanorods [11], this process being controlled by added surfactants, the concentration of the metal precursor, and the reaction temperature during the synthesis process. Moreover, such bimetallic species have been used for the decoration of other nanomaterials exhibiting semiconducting or quasi-metallic characters, such as SiO_2 [12], TiO_2 [13], $\text{TiO}_2/\text{MoS}_2$ [14], TiSi [15], CeO_2 [16], rGO [8], and $\text{g-C}_3\text{N}_4$ [17], providing improved photoresponse or catalytic properties, e.g. towards methanol oxidation or the reduction of dioxygen and hydrogen peroxide [18].

Nevertheless, in spite of the various synthesis methods and modifications based on wet-chemistry routes [19], all of the procedures lead to the formation of colloid that after some time can aggregate because of the high surface energy of the NPs. Following that, activity can be lost as further usage as an electrode material requires immobilisation onto the conductive support. Thus, for electrocatalytic and photoelectrochemical reactions, a uniform distribution of nanoparticles onto the substrate should be achieved. Typically, transparent metal oxide (FTO, ITO), glassy carbon [20], or carbon paper [21] as a charge collector have been proposed, while optimised spin-coating, dip-coating, or electrochemical deposition were utilised for the preparation of the complete electrode material. Another way to form an electrode with an already-anchored bimetallic nanostructure on a stable surface is via rapid thermal annealing of sputtered thin metallic films [22]. Thin metal film dewetting is a simple route for the formation of nanoparticles. Their size can be tuned by changing the annealing temperature, atmosphere, or initial film thickness. The annealing process can be divided into conventional furnace annealing (CFA), and rapid thermal annealing (RTA). RTA has many advantages over CFA such as lower dewetting temperatures of thin metal films with an increase of heating rate, lower crystallisation temperature, minimised film substrate interface reactions, shorter annealing time, better electrical properties, and reduced thermal costs [23]. According to Bergum et al. [24], rapid thermal annealing of thin layers of Cu_2O prepared using magnetron sputtering improves their carrier transport, while Kumar et al. [25] reported that RTA, owing to the faster heating rates, shorter time, and lower temperatures, promotes the formation of a smaller grain size of Cu and Ag–Cu materials. Moreover, Khaoo et al. [26] achieved an increase in photovoltaic performance and external quantum efficiency for $\text{ZnO}/\text{Cu}_2\text{O}$ by rapid thermal annealing. The number of grain boundaries decreased while the number of pores increased simultaneously with the temperature growth. In such a case, a more porous structure with carrier recombination sites is formed due to the higher temperature. Films can be formed on a flat or textured substrate exhibiting a developed surface area that can also limit the size of the formed nanoparticles and ensure a high degree of spatial ordering. In that case, the thermal conditions play a crucial role since the temperature stress is applied

both to the metallic film and the substrate, affecting its possible oxidation, and a change in the resistance of the whole material. Taking into account the increased available surface area, and the higher catalytic and electrocatalytic response, a semiconducting interlayer or matrix for further hosting of AuCu is frequently selected, such as titania [27], zinc oxide [28], carbon paste with nano P zeolite [29], or carbon nanofibre [30]. However, achieving a uniform distribution of NPs is especially challenging and therefore the reproducibility is poor. Focussing on photoreponsive electrode materials containing small metal species, the selection of TiO_2 is commonly recommended due to its semiconducting character ensuring efficient e–h pair separation, low-cost, non-toxicity, and corrosion resistance. However, its wide bandgap energy limits activity in the visible light spectrum, but further decoration by metal nanostructures can shift the absorbance of the material towards longer wavelengths, thereby improving the photoelectrochemical activity. Similar to the case where a wide bandgap semiconductor is modified by monometallic nanoparticles, surface plasmon resonance (SPR) [31] and the formation of a Schottky heterojunction are mainly responsible for the improved light-driven harvesting of electrochemical response, and the simultaneous suppression the recombination of photogenerated carriers [32, 33]. The mechanism of the photon-harvesting abilities exhibits a complex nature since it depends on the illumination side of the material, first titania and then AuCu nanoparticles, and vice versa [34] for a structure deposited onto a semitransparent substrate. When both a wide bandgap semiconductor and a bimetallic nanostructure are exposed to radiation at the same time, several phenomena occur. In such a case, the overall performance depends on the reaction dynamics, and smart but simple control of the morphology and internal structure can result in highly effective nanocatalytic platforms for organic transformations [35], CO_2 -to- CH_4 conversion [21], as well as light-driven current generation [32].

In this paper, we focus onto the precisely temperature-managed synthesis of nanomosaic material created by bimetallic AuCu nanostructures directly on a textured Ti substrate. The Ti substrate was produced by electrochemical anodisation resulting in the growth of ordered titania nanotubes (TiO_2NTs). After selective etching of titania, a platform composed of highly ordered titanium nanodimples

(TiNDs) remains. In order to obtain a AuCu nanomosaic, gold and copper layers in various sequences as well as a AuCu mixture were sputtered onto the Ti substrate. Finally, the samples were annealed at 100, 200, 300, 400, 500, and 600 °C in a rapid thermal annealing furnace (RTA) under an air atmosphere in contrast to the procedure where substrates are simply introduced into a preheated muffle furnace and removed after a certain period [36]. In our previous report, we showed only the behaviour of the material in two temperature regimes and the given results were just an announcement for further studies providing a wider overview regarding the outstanding features and perspective applications of AuCu bimetallic nanostructures. Thus, complex characterisation of the temperature-controlled morphology is carried out while the structural and optical features were examined using scanning electron microscopy and different spectroscopic techniques: X-ray diffraction, Raman, X-ray photoelectron, and UV–vis absorption spectroscopies. Moreover, the study shows the strong influence of the thermal annealing conditions on the electrochemical and photoelectrochemical performance of AuCu structures formed over a titanium support covered with a thin passivation TiO_2 layer.

2 Experimental

2.1 Reagents

Titanium foil (99.7%, thickness: 0.127 mm, Strem), acetone (Chempur), ethanol (96%, Chempur), ammonium fluoride (98%, Chempur), ethylene glycol (99%, Chempur), oxalic acid dihydrate (99.5%, Sigma-Aldrich), gold target (99.99%, Quorum Technologies), copper target (99.99%, Quorum Technologies), and gold/copper alloy target (Au50/Cu50 At%, Goodfellow).

2.2 AuCu electrode fabrication

The Ti foil was cut into $2 \times 3 \text{ cm}^2$ plates and ultrasonically cleaned in acetone, ethanol, and water for 10 min. Then Ti was used for the electrochemical anodisation process. Anodisation was conducted in the two-electrode system, where the Ti was used as the anode, and a Pt mesh as the cathode. The electrodes were placed against at a distance of 2 cm from

each other in a cylindrical glass cell filled with electrolyte. The synthesis was based on two subsequent anodisations followed by chemical etching processes. The electrolyte contained 0.27 M NH_4F dissolved in a mixture composed of 1% vol. deionised water and 99% vol. ethylene glycol. The anodisation process was carried out in glass cells with a thermostated jacket at a voltage of 40 V, and a temperature of 23 °C for 2 h for the first stage, and 6 h for the second stage. After each anodisation stage, the formed TiO_2 nanotubes were chemically etched overnight in 0.5% oxalic acid solution in glass beakers, and afterwards the samples were rinsed with deionised water. A complete description of the applied procedures can be found elsewhere [37, 38]. As a result, a honeycomb structure composed of closely packed dimples of a diameter corresponding to the external diameter of the nanotubes was formed, and labelled as TiND. The obtained platform was used during magnetron sputtering (Q150T S system, Quorum Technologies) of 10 nm of AuCu alloy (in the manuscript, assigned as 10AuCu) as well as 5 nm layers of Au and Cu in both sequences (assigned as 5AuCu and 5CuAu, respectively). The non-annealed samples were labelled as NA. Afterwards, the electrodes were thermally treated in a Rapid Thermal Annealing furnace (MILA 5000 P-N) for 30 min in air with a heating rate of 45 °C/s. The modifications of different samples were carried out at 100, 200, 300, 400, 500, and 600 °C.

2.3 Sample characterisation

The morphology of the prepared samples was investigated by a field emission scanning electron microscope (FEI Quanta FEG250) equipped with a secondary ET detector and with the beam accelerating voltage kept at 10 kV. The optical properties of the nanostructures were inspected using a UV-vis spectrophotometer (Lambda 35, Perkin-Elmer) equipped with a diffuse reflectance accessory. The spectra were registered in the range of 300–1000 nm with a scanning speed of 60 nm/min. The crystal structure of the 10AuCu sample was verified by X-ray diffraction over the range of 20–80 degrees using a Bruker 2D Phaser diffractometer with $\text{CuK}\alpha$ radiation and an XE-T detector. The Raman spectra were recorded by means of a confocal micro-Raman spectrometer (InVia, Renishaw) with sample excitation by an argon ion laser emitting at 514 nm and operating at 50% of its total power. The chemical

nature of the samples was studied by an X-ray photoelectron spectroscope (Escalab 250Xi, ThermoFisher Scientific) with a monochromatic $\text{AlK}\alpha$ source. The high resolution spectra of $\text{Au}4f$, $\text{Cu}2p$, $\text{Ti}2p$, and $\text{O}1s$ for the 10AuCu electrode were captured. The electrochemical and photoelectrochemical properties were measured using an AutoLab PGStat 302 N potentiostat–galvanostat in the three-electrode assembly, where the titanium substrate modified by gold–copper structures was the working electrode (WE), Ag/AgCl/0.1 M KCl served as the reference electrode (RE), and a Pt mesh was the counter electrode (CE). Cyclic voltammetry and linear voltammetry measurements were carried out in deaerated 0.1 M NaOH electrolyte. The cyclic voltammetry (CV) curves were registered within the range from -0.5 towards $+0.5$ V with a scan rate of 50 mV/s, while the linear voltammetry (LV) scans were performed across a wider potential range from -0.8 to $+0.8$ V with a scan rate of 10 mV/s. The LV curves were recorded in the dark and under illumination with a xenon lamp (LOT-QuantumDesign GmbH) as a light source. The chronoamperometry measurements (CA) under chopped light were performed at $+0.3$ V during 200 s. The 3D map of the photocurrent density was registered by photoelectric spectrometer (Instytut Fotonowy) equipped with Xe lamp 150 W. The curves were recorded at the potential range from -0.8 to $+0.8$ V and wavelengths from 300 to 700 nm. The measurement was carried out in 0.1 M NaOH solution in three-electrode system where 10AuCu electrode was the WE, Ag/AgCl/0.1 M KCl was the RE, and Pt wire served as the CE.

3 Results and discussion

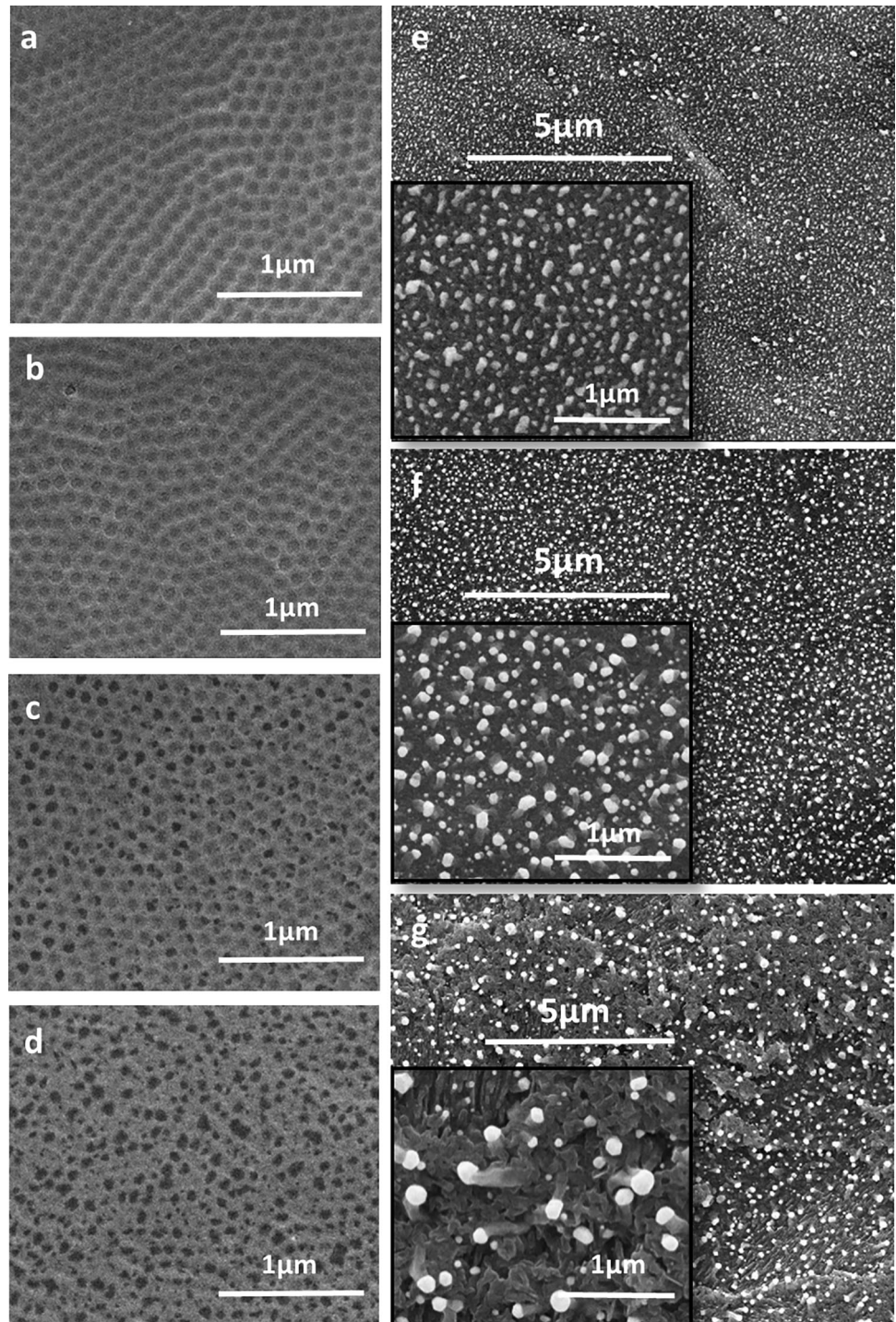
3.1 Morphology

SEM images of the fabricated samples composed of gold–copper structures on a nanotextured titanium substrate are shown in Fig. 1. Of all of the prepared samples, the 10AuCu alloy was selected for detailed analysis, due to it having the best electrochemical results, which will be discussed further on. As can be observed, thermal annealing strongly affected the morphology of the electrodes. For electrodes without thermal treatment (Fig. 1a) or annealed at 100 °C (Fig. 1b) or 200 °C (Fig. 1c), the characteristic dimples

are clearly visible. The diameter of the dimples for the 10AuCu layer was estimated to be 76 ± 8 nm. Whereas, in our previous work, the diameter of closely packed Ti dimples without the AuCu layer and thermal treatment was reported to be 85 ± 3 nm [38]. With the temperature increase to 200 °C, the diameter of the nanodimples did not change significantly,

however, further growth of the temperature caused the gradual disappearance of the cavities (Fig. 1d). Similar to Grochowska et al. [34], the layer fragmentation started at the grain boundaries. At a temperature of 300 °C, islands of irregular shapes were created [39], while at 400 °C, AuCu nanoparticles formed. The resulting AuCu NPs were irregular in

Fig. 1 SEM images of 10AuCu electrode **a** without thermal treatment, and after thermal annealing at **b** 100 °C, **c** 200 °C, **d** 300 °C, **e** 400 °C, **f** 500 °C, **g** 600 °C



shape and the average size equalled 70 ± 34 nm. At the temperatures of 500 °C (Fig. 1e) and 600 °C (Fig. 1f), the fabricated nanoparticles became more spherical and the Ti nanodimples were no longer distinguished. The diameter of the AuCu NPs formed at 500 °C was 74 ± 28 nm, while those annealed at 600 °C were 123 ± 49 nm. As can be observed, the size of the nanoparticles as well as the standard deviation increased with the temperature. This may be related to the disappearance of the nanodimples as it is known that the presence of cavities in Ti foil ensures the formation of nanoparticles that are regularly distributed and quite regular in shape and size [40].

3.2 Optical properties

The differences in the annealing temperature of the AuCu nanostructures influenced colour changes of the electrode surface which can be observed by the naked eye (Fig. 2). A variety of colours from pearl (100 °C), gold brown (200, 300 °C), and violet (400 °C) to grey (600 °C) were obtained. According to Fredj et al., the temperature during the fabrication process is associated with changes in the colour of copper oxides films [41]. Moreover, the dependence between the appearance of the surface and the thickness of the created oxide was also evaluated. Additionally, the colour impression depending on the thickness of the Ti and TiO₂ layers was reported by L. Skowroński et al. [42]. Nevertheless, in our case, it was most likely the presence of copper, and

titanium and titanium dioxide that influenced the colour of the samples.

The reflectance spectra were recorded to reveal the optical properties of the 10AuCu, 5Au5Cu, and 5Cu5Au electrodes (Fig. 3). As can be observed, the shape of the spectrum changed because of the differences in the morphology caused by thermal dewetting, and the presence of the resulting gold–copper structure. From the SEM images, it can be observed that the AuCu nanostructures annealed below 200 °C preserved the periodic arrangement of Ti nanocavities, and possibly their geometry influenced the shape of the spectrum in the range from 300 to 600 nm [43]. The reflectance band minima for the 10AuCu, 5Au5Cu, and 5Cu5Au annealed at 200 °C were located at 390, 390, and 400 nm, respectively (Fig. 3d), while for 300 and 400 °C, they were shifted to c.a. 405, 475, and 420 nm, and 530, 520, and 540 nm, respectively (Fig. 3e). According to Guo et al. [44], the peak intensity and position are component-dependent for Au_xCu@TiO₂ structures, and are located at 430, 470, and 550 nm for Au₃Cu, AuCu, and AuCu₃ nanoparticles. In our previous studies, a shift in the absorbance maxima for gold–copper materials from 470 to 900 nm was revealed, and caused by changes in morphology after increasing the annealing temperature from 450 to 600 °C [36]. In that work, the temperature increase resulted in the formation of AuCu NPs on the surface of the substrate at 600 °C. The same phenomenon took place here, however, at a much lower temperature,

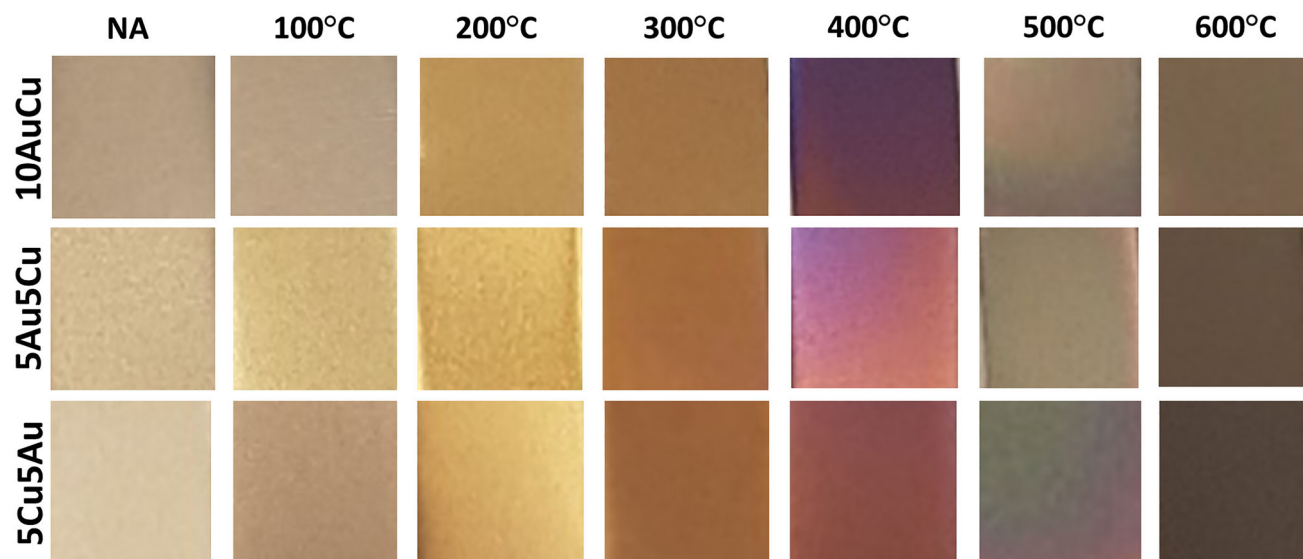


Fig. 2 Dependence of colour of the prepared samples on the annealing temperature

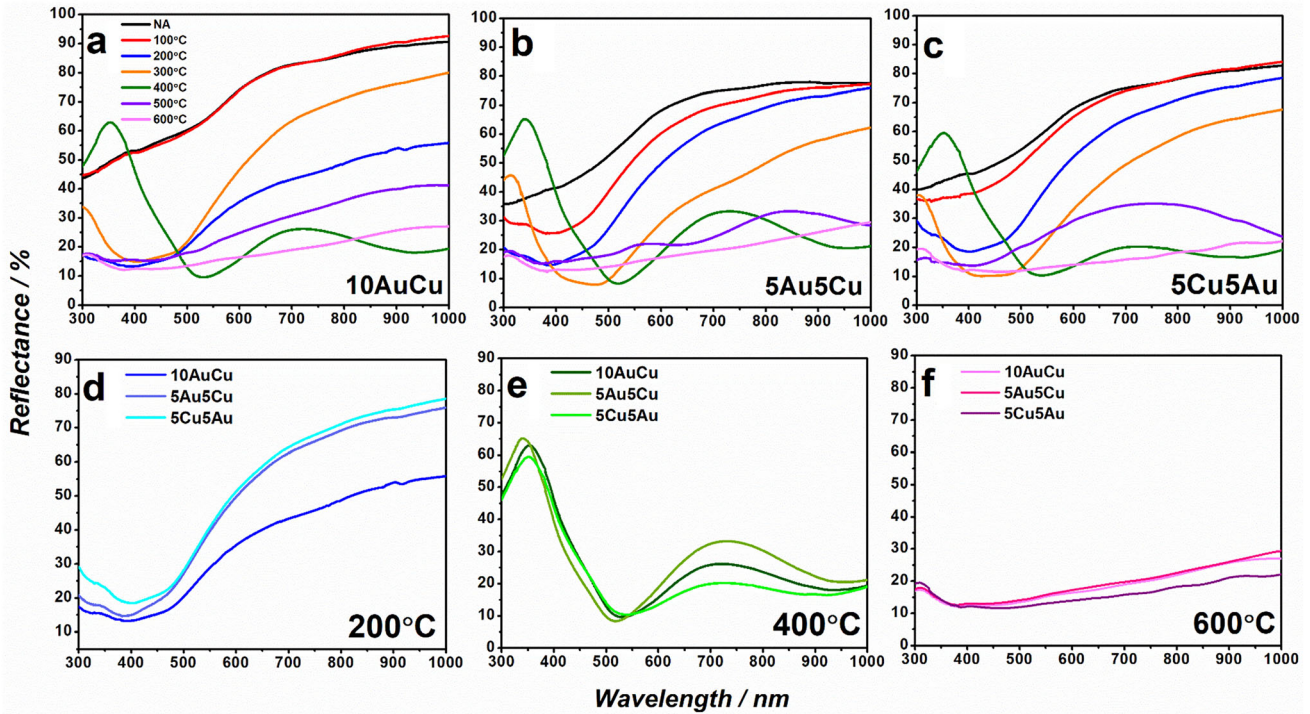


Fig. 3 Reflectance spectra of **a** 10AuCu, **b** 5Au5Cu, **c** 5Cu5Au and selected results for electrodes annealed at **d** 300 °C, **e** 400 °C, **f** 600 °C

namely 400 °C. Above this temperature, AuCu nanoparticles were formed on the surface, and broadband absorbance from c.a. 400 to 1000 nm was observed. According to Scaiano et al. [45], CuNPs show a surface plasmon absorption band between 575 and 580 nm. Nguyen et al. reported that AuNPs/TiO₂ nanostructures exhibited increased absorbance in the UV region below 380 nm, corresponding to the bandgap of anatase TiO₂, and in the visible light region from 490 to 650 nm, attributed to the SPR effect of AuNPs [46]. In our case, no anatase phase presence was demonstrated, however, the rutile phase for the materials fabricated at 500 and 600 °C was established from the Raman spectroscopy measurements. Even though the substrate was titanium on its surface, a passivation layer of TiO₂ was formed. The rutile was confirmed by XRD patterns not only for 500 and 600 °C, but also a small amount for 400 °C. With increasing the annealing temperature from 400 to 600 °C, a thicker layer of TiO₂ was formed on the surface. Therefore, a decrease in reflectance in the range from 300 to 400 nm above 400 °C may be found [47]. As can be observed, the annealing of the 10AuCu, 5Au5Cu, and 5Cu5Au samples at 600 °C resulted in wide absorbance from 300 to 1000 nm (Fig. 3f).

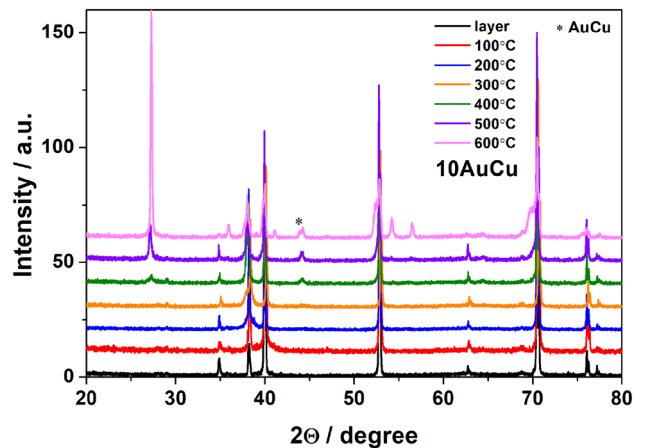


Fig. 4 XRD pattern of 10AuCu electrode annealed at different temperatures

3.3 Composition and crystallinity

The XRD diffraction patterns of the 10AuCu electrodes annealed at different temperatures are shown in Fig. 4. The peaks located at 34.9, 38.3, 39.9, 52.8, 62.7, 70.4, 76.1, and 77.2 degrees can be associated with the (100), (002), (101), (102), (110), (103), (112), and (201) planes of Ti [48], and only those peaks are present in the case of the electrode without annealing

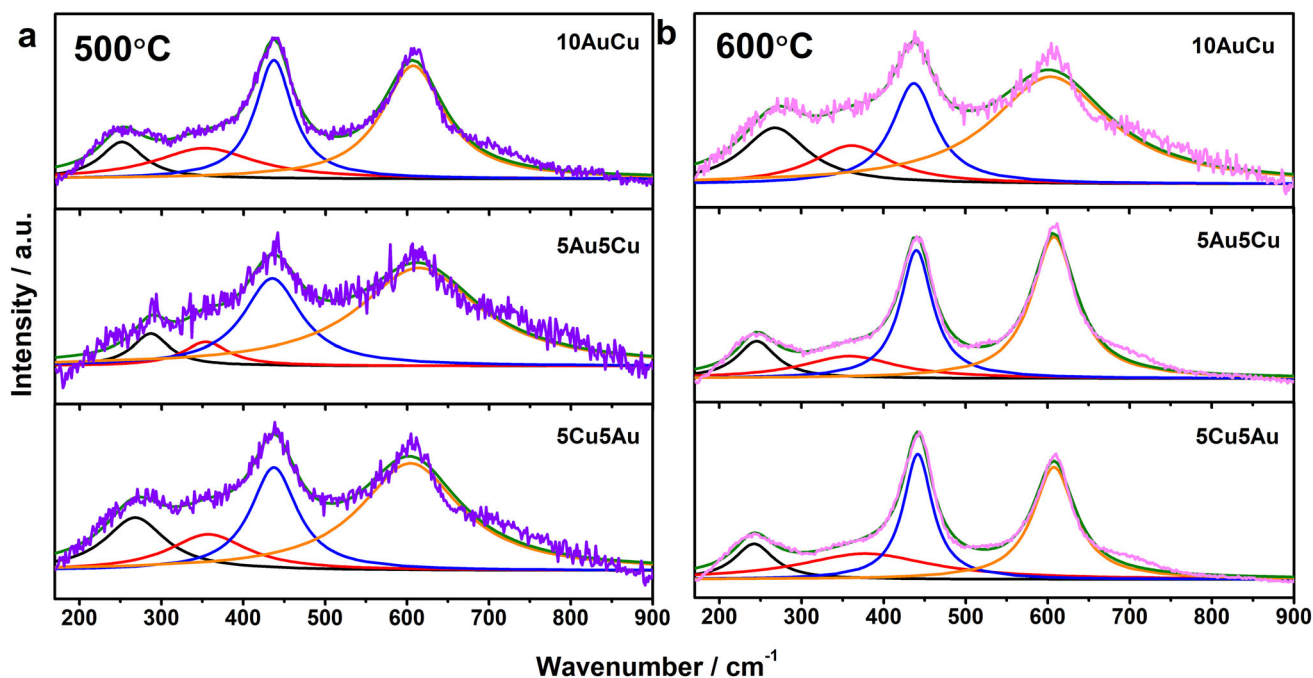


Fig. 5 Raman spectra of the samples annealed at **a** 500 °C and **b** 600 °C

and the ones treated up to 300 °C. When the temperature exceeded 400 °C, peaks at 27.3, and 44.2 degrees appeared, and they can be ascribed to the (110), and (210) planes of rutile. Moreover, the peaks already assigned to titanium foil are broadened, as the (002), and (301) rutile planes can be registered at 62.5, and 69.8 degrees. With the sample heated up to 600 °C, peaks related to the (101), (111), (211), (220), and (310) rutile planes arose, and the corresponding positions are 35.9, 41.1, 54.2, 56.5, and 64.5 degrees, respectively [49]. Additionally, with the increase of the rutile phase in the samples, pronounced broadening of the Ti peak located at 70.4 degrees is observed, as the 69.8 degrees peak of rutile is more intense. The increment of the rutile signal with the temperature growth from 400 to 600 °C is in agreement with the work of Qian et al. [50]. The SEM images show the formation of AuCu NPs at these temperatures, and the subsequent exposure of the substrate may be related to the increase in the intensity of the rutile peak. It should also be mentioned that rutile is formed out of the amorphous TiO₂ passivation layer and growth of the thickness of the oxide layer is expected at higher temperatures. Moreover, for the 10AuCu samples annealed at 600 °C, a peak from AuCu can be observed [51].

More detailed characterisation of the structure of the samples was conducted based on Raman

measurements. The Raman spectra of the gold–copper structures on the Ti substrate annealed at 500, and 600 °C are shown in Fig. 5. These temperatures were selected based on the XRD measurements. It can be observed that not only the increase in temperature affects the Raman spectra but also the configuration of the gold and copper. Raman bands associated with AuCu can be found from 240 to 270 cm⁻¹ [52]. The location of CuO bands is calculated to occur in the 350–370 cm⁻¹ region [53]. According to Kalaivani and Anilkumar[54], bands located at c.a. 230, 440, and 605 cm⁻¹ can be ascribed to rutile. Nevertheless, based on the values collected in Table 1, determined using deconvolution, it can be observed that the band corresponding to AuCu for the 5Au5Cu and 5Cu5Au samples is redshifted after the increase of the temperature from 500 to 600 °C. Moreover, the largest shift of c.a. 40 cm⁻¹ was observed for the 5Au5Cu electrode. This phenomenon may occur because of the higher ratio between rutile and AuCu at 600 °C for this sample. The rutile bands can be found not only at 440 and 605 cm⁻¹, but are also probably hidden in the spectrum at 230 cm⁻¹. However, for the 10AuCu electrode, a shift for the AuCu compound from 252 to 268 cm⁻¹ can be observed. The blue shift may be caused by the formation of a higher amount of CuO species from gold–copper alloy after increasing the temperature from 500 to 600 °C. This

Table 1 Location of Raman bands derived from Fig. 5

Compound	Temperature/°C	Raman shifts/cm ⁻¹			References
		10AuCu	5Au5Cu	5Cu5Au	
AuCu	500	252	287	268	[47]
	600	268	246	242	
CuO	500	353	354	357	[48]
	600	361	359	378	
Rutile	500	437	435	437	[49]
		607	615	603	
	600	437	440	442	
		604	608	608	

phenomenon can dominate over rutile formation. The blueshift of the band associated with CuO after thermal treatment at 600 °C can be ascribed to the enhancement of interactions between the CuO and rutile phases. In Mosquera et al. [55], the shift of the Raman band was observed for rutile from 235 to 245 cm⁻¹ during temperature changes.

3.4 Characterisation of the chemical nature of the samples

XPS measurements were conducted to track the chemical character of the 10AuCu electrode. Figure 6 presents the XPS spectra for the electrodes annealed at 200, 300, 400, and 500 °C. The obtained results are summarised in Table 2. Moreover, the changes in the proportion of the elements/compounds in the studied materials depending on the temperature are shown in Fig. 7. The spectrum for *Au4f* appears as a peak doublet (Fig. 6a) located at - 84.0 and - 87.5 eV, and confirmed the presence of metallic Au [56]. The Au At% increases with the increase in temperature, reaching the maximum at 400 °C (Fig. 7). In the case of copper, the *Cu2p* chemical states were analysed (Fig. 6b). For the electrodes annealed at 200, 300, and 400 °C, three chemical states were designated. The first, located at 932.6 eV is ascribed as Cu (AuCu)[57]. The second component, shifted by - 1.2 eV, is assigned to CuO. Finally, the component located at 935.2 eV is associated with Cu(OH)₂*-CuCO₃. For the 10AuCu electrode annealed at 500 °C, the presence of CuAuTi alloy is confirmed by the peak situated at 931.2 eV. The *Ti2p3/2* chemical state was not found for the sample annealed at 200 °C, which may be caused by the substrate being covered with a tight layer of AuCu. Above 300 °C, the TiO₂ (458.6 eV) At% increases with increasing temperature (Fig. 7) caused by the subsequent

exposure of the substrate. Last but not least, the analysis of the *O1s* spectrum is shown in Fig. 6d. The most notable component at - 529.7 eV should be related to the O²⁻ present in the 10AuCu electrode in the form of metal oxides. In addition, the peaks at 531.5 eV are linked to surface-adsorbed OH⁻ and Cu(OH)₂ [58].

To define the changes in the thickness of the passivation layer resulting from the formation of bimetallic 10AuCu structures (after thermal treatment at 400 °C), we carried out another XPS experiment, this time using Ar⁺ ions to provide a depth profile study. The results of this study are shown in Fig. S1. The 10AuCu electrode thermally treated at 400 °C was selected for detailed analysis, due to the presence of both AuCuNPs and TiNDs (Fig. 1e). Comparing the Ti foil and the 10AuCu electrode depth profiles allows us to draw some conclusions on the thickness of the passivation TiO₂ layer. The naturally grown oxides on the Ti foil are formed primarily of TiO₂ but also of some Ti₂O₃. Their share at the surface is over four times higher when compared with the 10AuCu sample, but the TiO₂ was present in both cases (see Fig. S1b). The surface *Ti2p3/2* spectrum recorded for the Ti foil is also composed of the metallic Ti component at 453.8 eV. This result testifies that the thickness of the native film is below 5 nm thick, considering the depth of photoelectron acquisition in XPS. The native oxide layer is removed from the Ti foil after - 40 s of argon ion bombardment, suggesting an approx. 0.12 nm/s etching rate in our case. From the changes in the depth profile at Fig. S1a, it should be concluded that for the 10AuCu sample, the TiO₂ oxide layer is dominant after roughly 100–440 s of ion bombardment, leading to the assumption that the passive layer is a few times thicker than the Ti foil. These changes should be explained by the calcination process modifying the

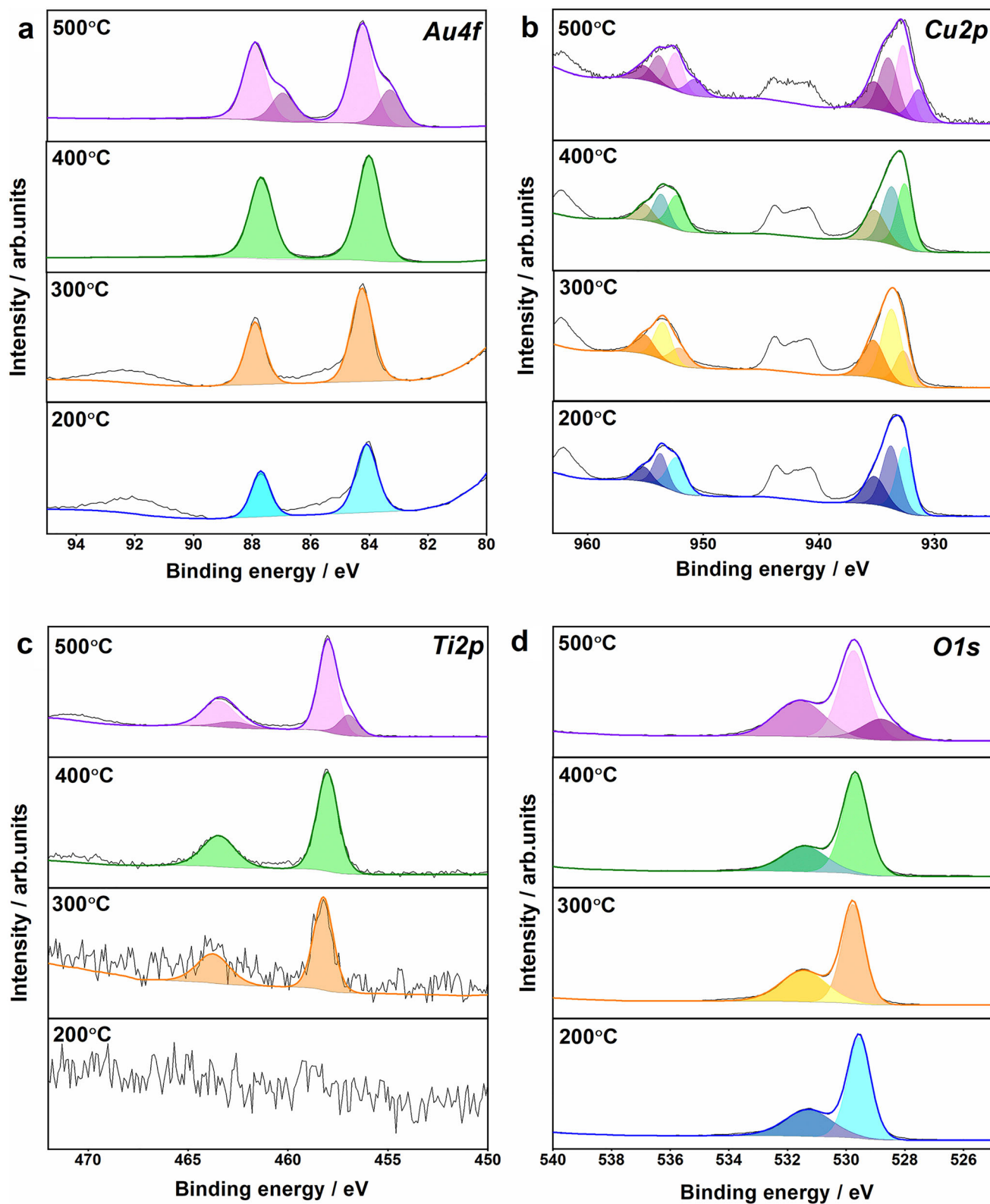


Fig. 6 XPS high-resolution spectra registered for 10AuCu electrode annealed at 200 °C, 300 °C, 400 °C, 500 °C: **a** *Au4f*, **b** *Cu2p*, **c** *Ti2p*, and **d** *O1s*

Table 2 Binding energies (BE) of 10AuCu electrodes: annealed at 200 °C, 300 °C, 400 °C, 500 °C

Peak	Component	BE/eV	At.%	Peak	Component	BE/eV	At.%
200 °C				200 °C			
Au4f 7/2	Au	84.1	0.83	Ti2p 3/2	–	–	–
300 °C				300 °C			
Au4f 7/2	Au	84.2	1.4	Ti2p 3/2	TiO ₂	458.6	0.6
400 °C				400 °C			
Au4f 7/2	Au	84.0	12.4	Ti2p 3/2	TiO ₂	458.4	4.4
500 °C				500 °C			
Au4f 7/2	Au (CuAuTi)	83.3	1.4	Ti2p 3/2	Ti (CuAuTi)	457.3	3.7
Au4f 7/2	Au	84.2	3.7	Ti2p 3/2	TiO ₂	458.4	15.6
200 °C				200 °C			
Cu2p 3/2	Cu (AuCu)	932.6	13.6	O1s	O ²⁻	529.5	44.6
Cu2p 3/2	CuO	933.8	14.6	O1s	OH ⁻	531.3	27.7
Cu2p 3/2	Cu(OH) ₂ *CuCO ₃	935.2	7.9				
300 °C				300 °C			
Cu2p 3/2	Cu (AuCu)	932.6	6.7	O1s	O ²⁻	529.8	41.1
Cu2p 3/2	CuO	933.6	16.7	O1s	OH ⁻	531.5	22.0
Cu2p 3/2	Cu(OH) ₂ *CuCO ₃	935.2	9.7				
400 °C				400 °C			
Cu2p 3/2	Cu (AuCu)	932.6	10.7	O1s	O ²⁻	529.7	37.8
Cu2p 3/2	CuO	933.8	11.1	O1s	OH ⁻	531.4	16.9
Cu2p 3/2	Cu(OH) ₂ *CuCO ₃	935.2	6.8				
500 °C				500 °C			
Cu2p 3/2	Cu (CuAuTi)	931.2	1.2	O1s	O ²⁻	528.8	10.9
Cu2p 3/2	Cu (AuCu)	932.5	2.2	O1s	O ²⁻	529.7	34.4
Cu2p 3/2	CuO	933.8	2.1	O1s	OH ⁻	531.6	23.6
Cu2p 3/2	Cu(OH) ₂ *CuCO ₃	935.0	1.3				

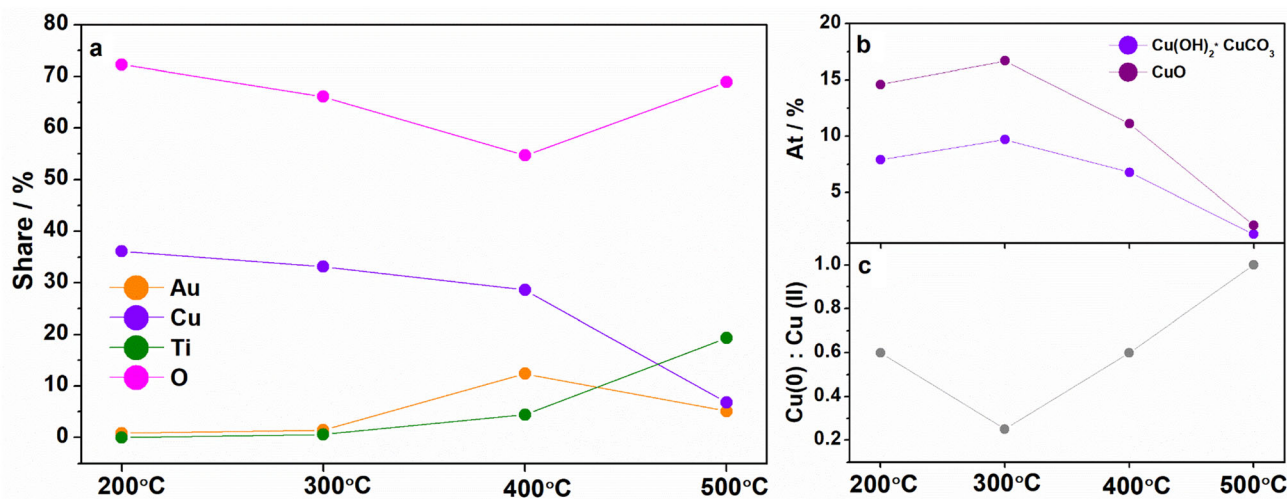


Fig. 7 Surface chemistry changes based on XPS analysis: **a** proportion of Au, Cu, Ti, and O elements as a result of annealing at different temperatures, **b** contribution of various Cu(II) species, **c** metallic Cu share

structure of the TiO₂ layer combined with some chemical changes within the layer. These are best observed in Fig. S1c, where the primary *Ti2p_{3/2}* spectral component is shifted from 458.7 eV,

characteristic of TiO₂, to 459.3 eV due to the formation of mixed (CuTi)O compounds.

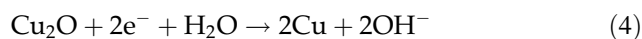
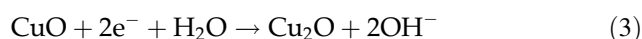
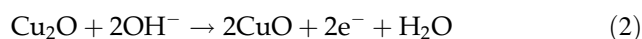
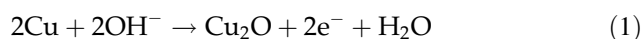
It should be kept in mind that depth profiling with XPS is subject to some level of uncertainty,

originating primarily from three factors. First, the etching rate for the pure TiO₂ of the Ti foil and the AuCu nanostructures is most certainly different. Thus the direct etch time comparison is flawed. Next, the titanium oxides tend to be reduced under the influence of the Ar⁺ ion gun leading to surface chemistry changes. For this reason, the share of both TiO₂ and Ti₂O₃ was summarised to present the depth profile in Fig. S1a. Finally, the ion gun is known to hammer some of the sample's atoms deeper into its structure rather than etching them, leading to the presence of some residual oxides even deep underneath the surface. For this reason, we subjectively recognised the limiting $Ti_{2p_{3/2}}$ TiO₂ share in the passive film to be – 15 at.%.

The XPS for 10AuCu electrode annealed at 500 °C after photoelectrochemical measurements together with the data analysis was added to Electronic Supporting Information (Fig. S2).

3.5 Electrochemical performance

The electrochemical activity of gold–copper structures with and without rapid thermal annealing was tested firstly using cyclic voltammetry in 0.1 M NaOH. The results obtained for bimetallic 10AuCu, 5Au5Cu, and 5Cu5Au electrodes are shown in Fig. 8. During the anodic potential scan, the oxidation of Cu (1) and Cu₂O (2) occurs, while during the reverse, cathodic scan, the reduction of copper oxides (3), (4) takes place [59]:



Regarding the 10AuCu sample before and after annealing at 100 °C, 200 °C, the visible oxidation peak (2) is present at ca. 0 V vs. Ag/AgCl/0.1 M KCl, and corresponds to the oxidation of Cu(I) to Cu(II). In addition, the peak observed at ca. – 0.1 V can be interpreted as the reduction of Cu(II) to Cu(I), and is labelled as (3). For the electrodes annealed at 300 °C and 400 °C, the abovementioned peaks are less intense, however, an additional reduction peak at + 0.1 V can also be found (5). This cathodic peak was ascribed by N. Shen et al. [60] to the reduction of Au₂O₃. For the electrodes annealed at 500 °C and 600 °C, no faradaic peaks were noticed. Moreover,

the recorded currents were much lower than those for the electrodes treated at temperatures equal to and lower than 400 °C, which may be caused by the increased resistivity of Ti at higher temperatures [61]. It should be noted that the 10AuCu samples annealed at 500 and 600 °C exhibit a very poor capacitive character. The CV recorded for the 5Au5Cu layer demonstrates two oxidation peaks, first at ca. – 0.15 V corresponding to the oxidation of Cu(0) to Cu(I) (1), and second at + 0.05 V established as the oxidation of Cu(I) to Cu(II) (2). The cathodic peaks observed at ca. – 0.1 and at – 0.4 V can be interpreted as a transformation of Cu(II) into Cu(I) (3), and Cu(I) into Cu(0) (4), respectively. The electrodes annealed at 100 and 200 °C behave similarly to the 10AuCu electrodes fabricated at this temperature. The 5Au5Cu electrode treated at 300 °C behaves differently than the 10AuCu and 5Cu5Au. Also, this phenomenon will be further observed in the case of the linear voltammetry scans shown in Fig. 10. From the temperature of 400 °C, no Faraday peaks are noticeable. In addition, the capacitive current increases when 600 °C is applied, which is related to the increase in the rutile content on the electrode surface, as indicated by XRD [62]. According to Salari et al. [63], the CV curves demonstrate the increase in capacitance with the increasing annealing temperature of TiO₂ NTs up to 600 °C because of the gradual growth of the share of rutile. Regarding the 5Cu5Au sample, for the non-annealed and those annealed at 100 and 200 °C, two anodic peaks can be observed at – 0.2 and at + 0.05 V vs. Ag/AgCl/0.1 M KCl, which can be assigned to the oxidation of Cu(0) to Cu(I) (1), and Cu(I) to Cu(II) (2), respectively. Furthermore, the cathodic signals at – 0.1 and – 0.45 V correspond to a reduction of Cu(II) to Cu(I) (3), and Cu(I) to Cu(0) (4), respectively. The 5Cu5Au electrode treated at 300 °C has the same electrochemical character of oxidation and reduction processes as the 10AuCu sample at this temperature. Similarly, to the 5Au5Cu, above 400 °C there are no Faraday peaks, and there is a rather poor capacitive character with low currents exhibited for the material treated at 500 and 600 °C. It should be noted that the electrochemical properties of each electrode, i.e. 10AuCu, 5Au5Cu, and 5Cu5Au, are related to the titanium substrate which is heated at the same time. The voltammetric curves for TiND annealed at different temperatures are shown in Fig. 8h. Within the investigated potential range, any Faradaic reaction

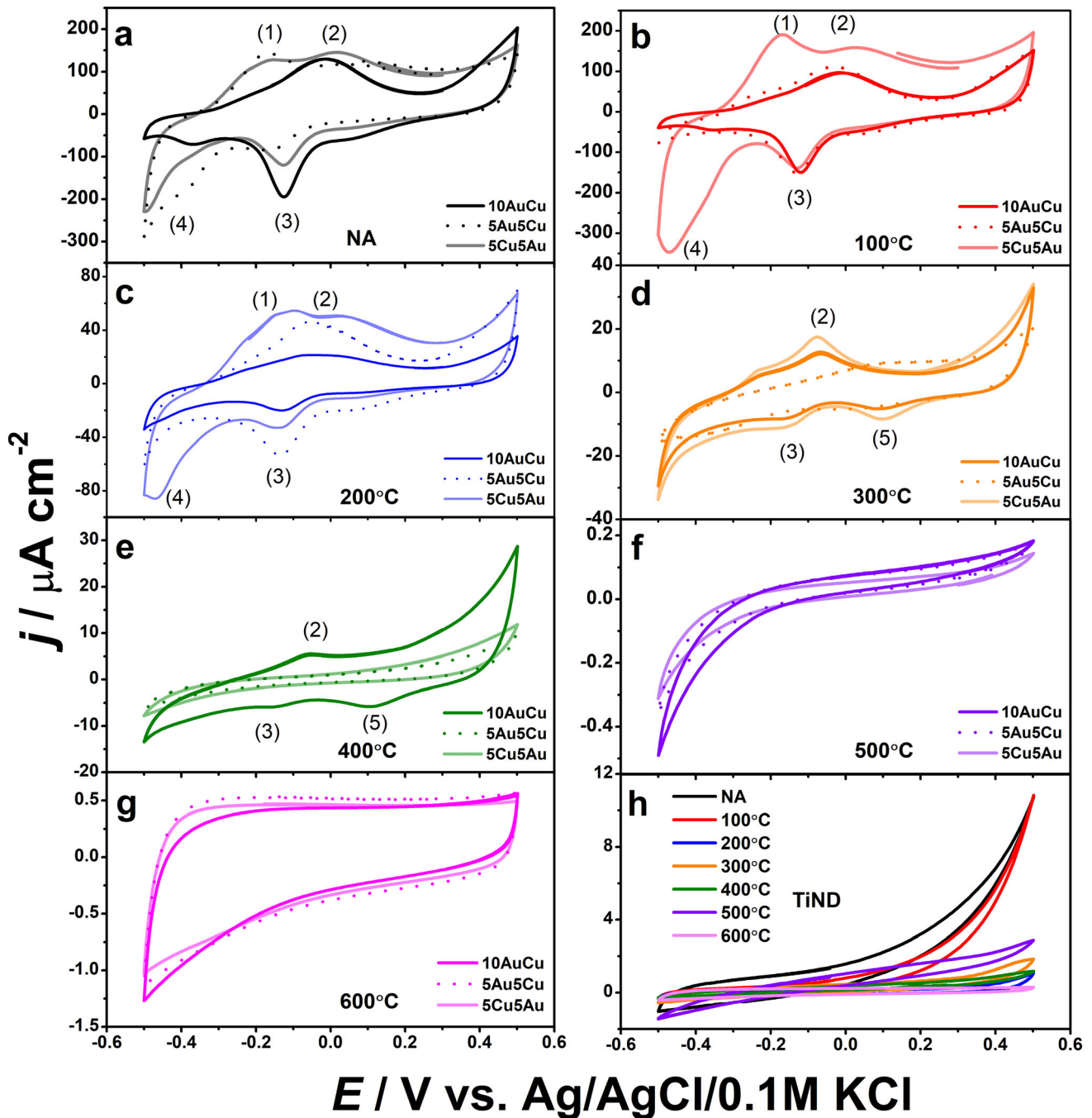


Fig. 8 Cyclic voltammograms registered in 0.1 M NaOH for 10AuCu, 5Au5Cu, 5Cu5Au electrodes **a** without annealing and thermally treated at **b** 100 °C, **c** 200 °C, **d** 300 °C, **e** 400 °C, **f** 500 °C, **g** 600 °C, and for **h** TiND substrate

was not recorded and only quite poor capacitive behaviour can be observed. Following that, up to 400 °C, the TiND as a supporting platform does not affect the electrochemical characteristics of bimetallic gold-copper structures. However, above this temperature, the titanium substrate significantly influences the material response. It can be observed in the

SEM images that at 500 °C and above, nanoparticles integrate with the titanium surface and the ordered Ti platform morphology is no longer seen. Such phenomena may be explained with the formation of $TiCu_3$ and Ti_3Cu_4 intermetallic phases, as was reported by Li et al. [64]. In our case, CuAuTi alloy was obtained.

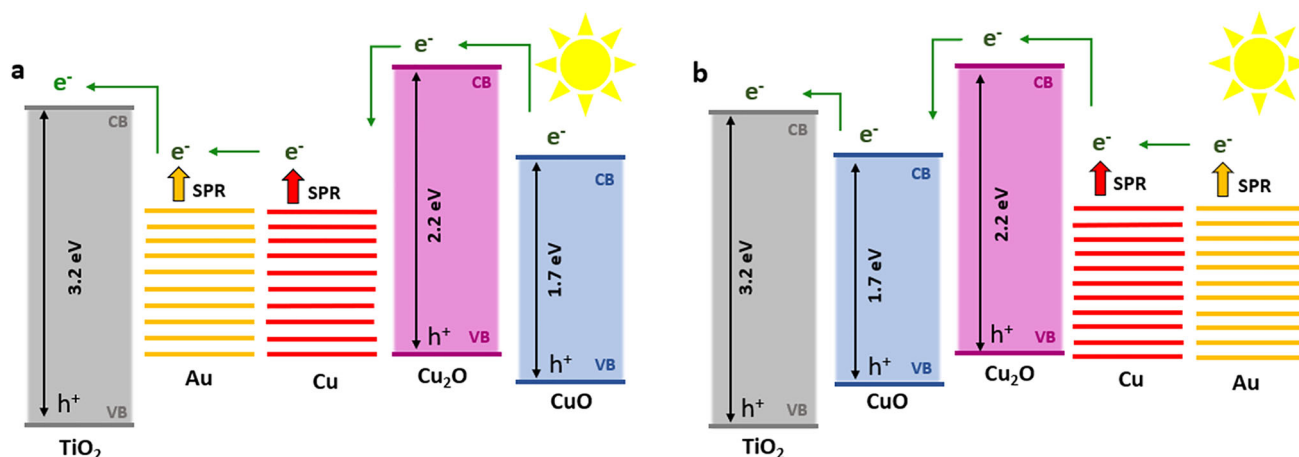


Fig. 9 Energy band diagrams in AuCu NPs on TiNDs when **a** gold is closer to TiO_2 , **b** copper oxides are closer to TiO_2

In order to examine the photoactivity of the fabricated nanostructures, linear voltammetry measurements in the dark, under UV–vis, and under visible illumination were performed. The temperature changes applied during thermal processing obviously influence the current density and the overall photoresponse of gold–copper nanomaterials. The signal in the cathodic potential regime when the electrodes were polarised at -0.8 V, and in the anodic regime at $+0.8$ V vs. Ag/AgCl/0.1 M KCl reached the maximum value at the particular temperature treatment. The comparison of the current densities recorded at -0.8 and $+0.8$ V under UV–vis illumination is given in Table 3. The maximum current density values recorded in the dark for each electrode material were obtained for temperatures in the range from 200 to 400 °C, which can be caused by the formation of the most catalytically active sites on gold–copper nanostructures. According to Tachikawa et al. [65], areal OER activity decreases as the annealing temperature increases from 300 to 450 °C due to the reduction in the number of catalytically active sites. The 5Au5Cu electrode annealed at 300 °C exhibits the highest value of current density at -0.8 V. However, at the potential of $+0.8$ V, the best result of 1.5 mA cm^{-2} was recorded for the 10AuCu sample also annealed at 300 °C. It should be mentioned that in the established anodic limit, any gas bubbles were not noticed at the electrode surface. According to our previous article [36], AuCu nanostructures annealed in a muffle furnace at 450 °C exhibit a high response towards OER with the intense evolution of gas bubbles. In that work, the current

density for 5Au/5Cu and 5Cu/5Au electrodes at $+0.8$ V vs. Ag/AgCl/0.1 M KCl under visible light illumination reached 1.32 and 1.26 mA cm^{-2} , respectively. For a more precise analysis, an additional measurement in the potential range from -0.8 to $+1.5$ V was performed for the 10AuCu electrode annealed in the RTA furnace at 300 °C (Fig. S3). The evolution of weak gas bubbles could be observed at $+1.2$ V. Therefore, two processes such as OER or oxidation of Cu^{2+} to Cu^{3+} [66] may take place at this potential.

In addition, the oxidation process enhanced by light took place at the potential of -0.17 V vs. Ag/AgCl/0.1 M KCl. The current densities are summarised in Table 4. This phenomenon occurs for a bimetallic gold–copper structure because of the synergistic effect [67]. It is possible that the increase in activity is related to the presence of copper oxides on top of the gold. This may be confirmed by the highest current value for the non-annealed 5Au5Cu electrode in which the topmost layer is copper. The greatest increase in the current recorded under UV–vis illumination between non-annealed and the thermally treated sample at -0.17 V was achieved by the 10AuCu electrode annealed at 300 °C (see Fig. 11a). The value increases from 31.2 to $349.1 \text{ } \mu\text{A cm}^{-2}$ which results in a current density 11 times higher than for a non-annealed nanostructure.

In order to analyse the changes caused by light, it is important to underline that when Cu_2O and TiO_2 semiconductors are connected, a p–n heterojunction can be formed [68]. The character of this junction is exhibited at the potential of ca. -0.3 V for electrodes

Table 3 Values of current density at -0.8 V and $+0.8$ V vs. Ag/AgCl/0.1 M KCl under UV-vis illumination for bimetallic nanostructures

	Current density at -0.8 V/mA cm ⁻²			Current density at $+0.8$ V/mA cm ⁻²		
	10AuCu	5Au5Cu	5Cu5Au	10AuCu	5Au5Cu	5Cu5Au
NA	-0.08	-0.15	-0.1	0.83	0.88	1.22
100 °C	-0.09	-0.16	-0.02	0.73	0.92	1.21
200 °C	-0.15	-0.16	-0.15	1.27	1.37	1.38
300 °C	-0.14	-0.38	-0.02	1.5	0.11	1.49
400 °C	-0.34	-0.09	-0.1	0.53	0.03	0.03
500 °C	-0.009	-0.006	-0.007	0.05	0.06	0.06
600 °C	-0.00003	0.004	-0.0004	0.08	0.1	0.07

Bold values indicate the highest current density obtained for the specific electrode (10AuCu, 5Au5Cu, 5Cu5Au) at the particular potential

Table 4 Values of current density at -0.17 V vs. Ag/AgCl/0.1 M KCl under UV-vis illumination for bimetallic nanostructures

	j at -0.17 V/ μ A cm ⁻²						
	NA	100 °C	200 °C	300 °C	400 °C	500 °C	600 °C
10AuCu	31.2	54.5	299.8	349.1	77.8	-0.5	0.1
5Au5Cu	233.8	141.4	152.5	30.4	1.9	-0.3	0.3
5Cu5Au	119.2	192.2	182.5	370.0	1.8	-0.3	0.1

Bold values indicate the highest current density obtained for the specific electrode 10AuCu, 5Au5Cu and 5Cu5Au at -0.17 V

annealed at 400 °C, and also for the 5Au5Cu sample thermally treated at 300 °C. A noticeable photocurrent response with efficient e-h pair separation [69] at 500 and 600 °C can be observed in Fig. 9. It can be assigned to the formation of a TiO₂ crystalline phase on the surface of the electrodes, as confirmed by the XRD and Raman measurements, in contrast to the materials annealed below 400 °C, where no rapid current increase and decrease is observed. The change in the current does not track the change in the light, and charge is accumulated at a potential of -0.17 V. The current densities recorded at $+0.3$ V vs. Ag/AgCl/0.1 M KCl for the 10AuCu, 5Au5Cu, and 5Cu5Au electrodes without and with thermal annealing at 500 and 600 °C are listed in Table 5. In our case, the highest value of photocurrent (91.4 μ A cm⁻²) was achieved for the 5Au5Cu sample annealed at 600 °C. The stability tests using CA for 10AuCu, 5Au5Cu, and 5Cu5Au electrodes annealed at 600 °C at $+0.3$ V are shown in Figure S4. The run of photocurrent indicates high photostability of the material under intermitted lighting. Due to UV-vis light irradiation, photogenerated electron-hole pairs are created in the TiO₂, Cu₂O, and CuO [67, 70]. At the same time, the Au and Cu generate hot electrons. It is possible that a more efficient electron transfer

Table 5 Values of current density at $+0.3$ V vs. Ag/AgCl/0.1 M KCl under UV-vis illumination for bimetallic nanostructures

Sample	Temperature/°C	j/ μ A cm ⁻²
10AuCu	NA	14.3
	500	47.7
	600	75.7
5Au5Cu	NA	17.6
	500	49.4
	600	91.4
5Cu5Au	NA	39.3
	500	50.9
	600	64.3

Bold value indicates the highest current density of all electrodes annealed at 500 and 600 °C obtained at $+0.3$ V

process can be found when the gold is closer to the TiO₂, and the copper oxides are on the surface CuO \rightarrow Cu₂O \rightarrow AuCu \rightarrow TiO₂ (Fig. 10). In our case, in one nanoparticle, a mixture of the abovementioned components is present, however, for the 5Au5Cu electrode configuration CuO/Cu₂O/AuCu/TiO₂ can dominate. According to Oh et al. [13], Au/Cu₂O core-shell NPs on TiO₂ nanorods, in which Au nanoparticles are the core while Cu₂O is the shell, can enhance photocatalytic activity. This may indicate

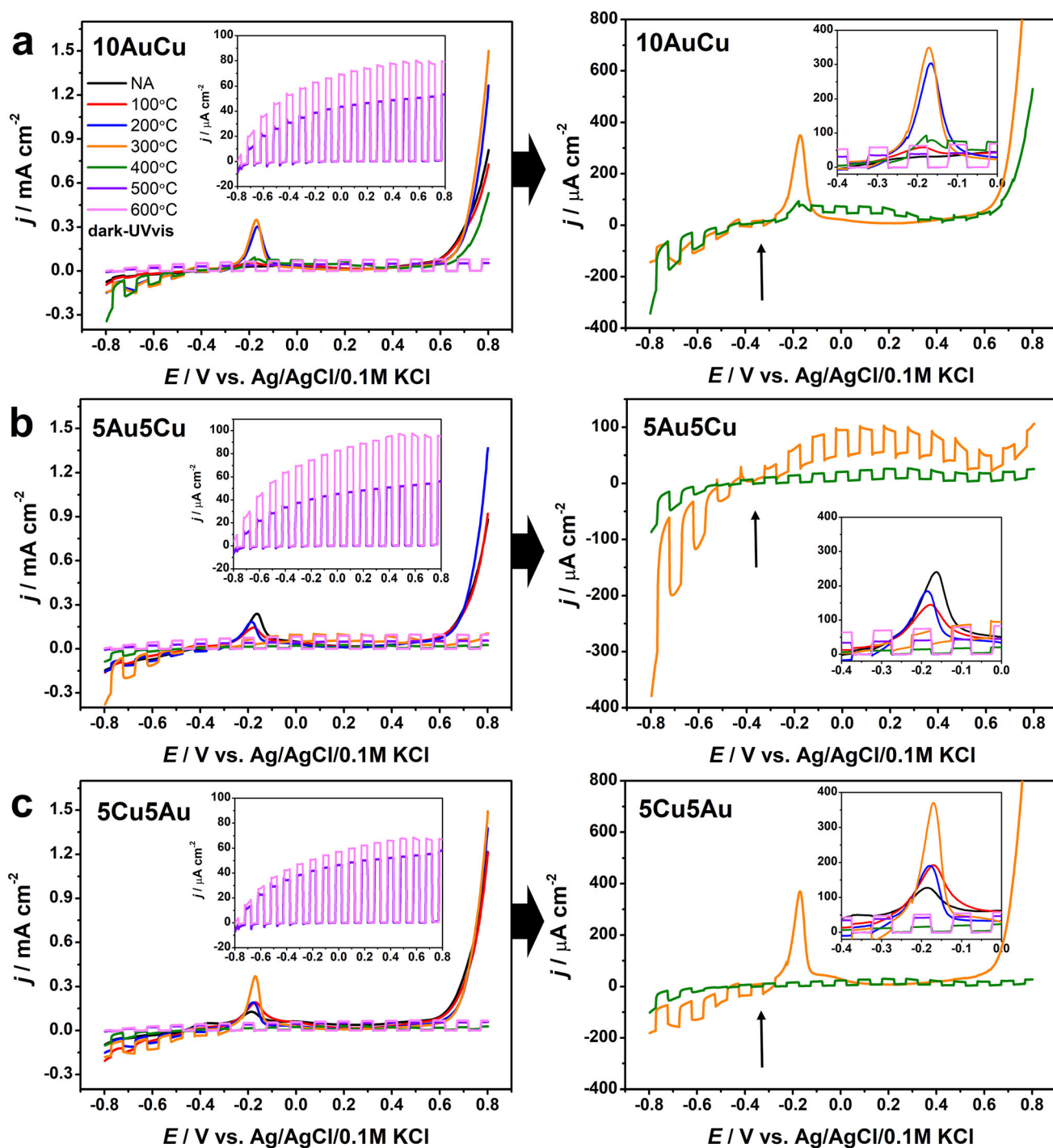


Fig. 10 Linear voltammetry curves registered in 0.1 M NaOH under UV-vis illumination for **a** 10AuCu, **b** 5Au5Cu, **c** 5Cu5Au electrodes annealed at different temperatures

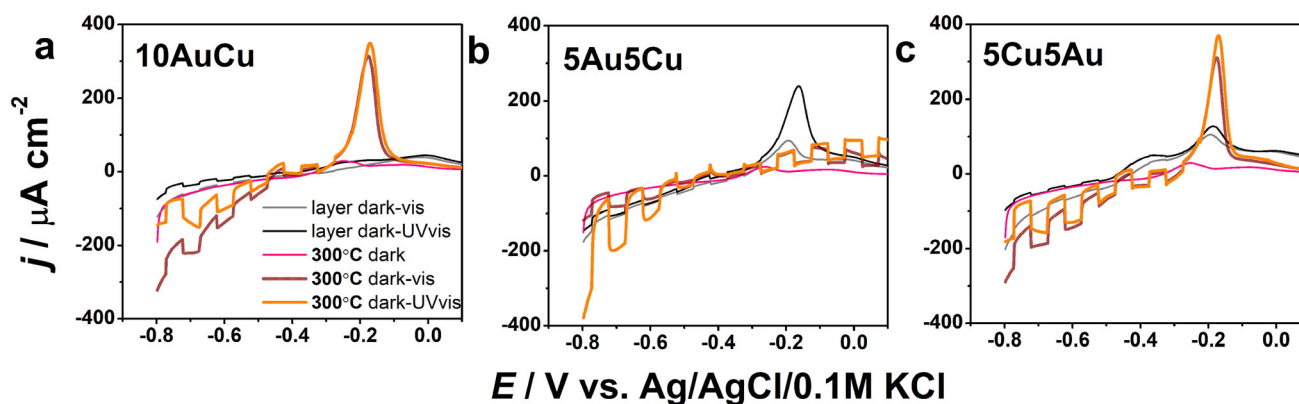
that photocurrent enhancement is in favour of samples that contain copper species on the top.

The comparison of photocurrent density values for fabricated electrodes and for various materials containing Au and copper oxides are listed in Table 6. The photocurrent density of the 5Au5Cu electrode is

higher than for Au@TiO₂/Cu₂O and AR-10AuCu/TiO₂NTs samples. In the case of the 5Au5Cu electrode, there is only a thin layer of TiO₂ which comes from naturally grown oxide onto the patterned Ti foil, whereas Au@TiO₂/Cu₂O and AR-10AuCu/TiO₂NTs are based on TiO₂ nanorods or TiO₂ nanotubes. The

Table 6 Values of photocurrent density for materials containing Au and copper oxides

Electrode material	Photocurrent density/ $\mu\text{A cm}^{-2}$	Potential/V vs. Ag/AgCl/0.1 M KCl	Electrolyte	References
Au@TiO ₂ /Cu ₂ O	17	+ 0.5	0.1 M PBS	[68]
AR-10AuCu/TiO ₂ NTs	64	- 0.2	0.1 M NaOH	[71]
Au_ZnO:Cu NRs	750	- 0.1	0.5 M Na ₂ SO ₄	[28]
10AuCu	76	+ 0.3	0.1 M NaOH	This work
5Au5Cu	91	+ 0.3	0.1 M NaOH	This work
5Cu5Au	64	+ 0.3	0.1 M NaOH	This work

**Fig. 11** Linear voltammetry curves registered in 0.1 M NaOH under visible and UV-vis illumination for **a** 10AuCu, **b** 5Au5Cu, **c** 5Cu5Au without and with thermal treatment at 300 °C

highest value of photocurrent density which equals to $750 \mu\text{A cm}^{-2}$ was obtained for Au_ZnO:Cu NRs, however, copper is not in the form of nanoparticles but as a dopant introduced into the structure of ZnO nanorods.

The 3D map of the photocurrent density was registered for the 10AuCu electrode annealed at 600 °C at the potential range from -0.8 to +0.8 V and wavelengths between 300 and 700 nm (Fig. S5a). As can be observed in the 3D curve the photocurrent grows when electrode is polarised towards anodic direction in the region of wavelengths between ca. 300 and 400 nm. The graph presented in Fig. S5b shows both absorbance spectra and the photocurrent spectra recorded at +0.3 V vs. Ag/AgCl/0.1 M KCl. As can be observed within the range between 300 and 430 nm, electrons are effectively converted into photocurrent. Within this region, the maximum of the photocurrent value was obtained when the light of 370 nm irradiates the electrode material.

Activity could be observed at the potential of -0.17 V vs. Ag/AgCl/0.1 M KCl for the bimetallic nanostructures not only under UV-vis illumination,

but also when the electrode surface was exposed to visible light (Fig. 11). As was mentioned before, the highest current value was achieved by the 10AuCu electrode. The sample is also active under visible light illumination, and this is equal to 0.3 mA cm^{-2} . This phenomenon can be related to the presence of Cu₂O, and CuO, which are p-type visible-active-light materials, and their stabilisation by Au after thermal annealing.

4 Conclusion

In this work, we proposed a fabrication procedure of a nanomosaic material composed of AuCu nanostructures located on a Ti nanotextured substrate. The TiND platform was fabricated via the electrochemical anodisation and chemical etching processes. The substrate was then covered by thin metal layers of AuCu mixture as well as Au and Cu in various sequences. The nanomaterials were modified in a RTA furnace heated to a temperature of 100, 200, 300, 400, 500, and 600 °C, and compared with the non-

annealed substrate. The different temperatures of thermal treatment had a significant impact on the morphology, optical, structural, and electrochemical properties. At a temperature of 400 °C, AuCu NPs are formed on the surface, and the size of these nanoparticles increases with the temperature. XRD and Raman spectroscopy measurements confirmed the formation of a rutile phase from the amorphous TiO₂ passivation layer on the electrodes annealed at 500 and 600 °C. For the samples thermally treated at 600 °C, wide absorbance from 300 to 1000 nm was obtained. The electrochemical and photoelectrochemical activity of all samples were measured using cyclic and linear voltammetry techniques in 0.1 M NaOH. The peaks of the oxidation of Cu(0) to Cu(I), and Cu(I) to Cu(II), as well as the reduction of Cu(II) to Cu(I), and Cu(I) to Cu(0) were visible for the samples annealed below 400 °C. An oxidation process enhanced by light caused by a synergistic effect of the combination of AuCu took place at -0.17 V vs. Ag/AgCl/0.1 M KCl. The 10AuCu electrode annealed at 300 °C achieved a current density 11 times higher than that recorded for the non-annealed nanostructure. We believe that the proposed approach can be extended to other platforms exhibiting a high degree of ordering, and therefore provides new opportunities in designing advanced photoactive materials.

Acknowledgements

The research is financed by the National Science Centre (Poland): Grant No. 2019/35/N/ST5/02604.

Author contribution

WL: Investigation, Validation, Conceptualisation, Writing—original draft, Writing—review & editing, Visualisation, and Funding acquisition. KG: Writing—original draft, Writing—review & editing, and Supervision. JK: Investigation, Validation, and Writing—review & editing. JR: Investigation, Validation, and Writing—review & editing. KS: Conceptualisation, Writing—original draft, Writing—review & editing, Supervision, and Funding acquisition.

Data availability

The datasets generated during and/or analysed during the current study are available from the corresponding author on reasonable request.

Declarations

Conflict of interest The authors declare that there is no conflict of interest.

Supplementary Information: The online version contains supplementary material available at <http://doi.org/10.1007/s10854-022-08775-9>.

Open Access This article is licensed under a Creative Commons Attribution 4.0 International License, which permits use, sharing, adaptation, distribution and reproduction in any medium or format, as long as you give appropriate credit to the original author(s) and the source, provide a link to the Creative Commons licence, and indicate if changes were made. The images or other third party material in this article are included in the article's Creative Commons licence, unless indicated otherwise in a credit line to the material. If material is not included in the article's Creative Commons licence and your intended use is not permitted by statutory regulation or exceeds the permitted use, you will need to obtain permission directly from the copyright holder. To view a copy of this licence, visit <http://creativecommons.org/licenses/by/4.0/>.

Supplementary Information: The online version contains supplementary material available at <http://doi.org/10.1007/s10854-022-08775-9>.

References

1. A.K. Sra, R.E. Schaak, *J. Am. Chem. Soc.* **126**, 6667–6672 (2004)
2. S. Thota, Y. Wang, J. Zhao, *Mater. Chem. Front.* **2**, 1074–1089 (2018)
3. P. Suchomel, L. Kvitek, R. Prucek, A. Panacek, A. Halder, S. Vajda, R. Zboril, *Sci. Rep.* **8**, 4589–4600 (2018)
4. S. Hussain, N. Kongi, H. Erikson, M. Rähn, M. Merisalu, L. Matisen, N. Alonso-Vante, *Electrochim. Acta* **316**, 162–172 (2019)
5. P. Kupracz, E. Coy, K. Grochowska, J. Karczewski, J. Rysz, K. Siuzdak, *Appl. Surf. Sci.* **530**, 147097–147107 (2020)

6. R. Singh, S. Dutta, *Adv. Powder Technol.* **29**, 211–219 (2018)
7. Y. Liu, Y. Liu, R. Yan, Y. Gao, P. Wang, *Electrochim. Acta* **331**, 135370 (2019)
8. L. Rout, A. Kumar, R.S. Dhaka, G.N. Reddy, S. Giri, P. Dash, *Appl. Catal. A* **538**, 107–122 (2017)
9. Q.Y. Liu, Y. Zhong, Z.Z. Jiang, K. Chen, S. Ma, P.F. Wang, Q. Wang, *J. Mater. Chem. C* **8**, 4869–4875 (2020)
10. R. Mendoza-Cruz, L. Bazán-Díaz, J.J. Velázquez-Salazar, J.E. Samaniego-Benitez, F.M. Ascencio-Aguirre, R. Herrera-Becerra, M. Jose-Yacamán, G. Guisbiers, *Nanoscale* **9**, 9267–9274 (2017)
11. J. Wang, X. Wu, W. Ma, C. Xu, *Adv. Func. Mater.* **30**, 2000670–2000680 (2020)
12. S. Schünemann, G. Dodekatos, H. Tüysüz, *Chem. Mater.* **27**, 7743–7750 (2015)
13. J.T. Oh, S.R. Chowdhury, T. Lee, M. Misra, *Dyes Pigm.* **160**, 936–943 (2019)
14. Y. Liu, Ch. Xu, Y. Xie, L. Yang, Y. Ling, L. Chen, *J. Alloy. Compd.* **820**, 153440–153448 (2020)
15. I. Barroso-Martín, E. Moretti, A. Talon, L. Storaro, E. Rodríguez-Castellón, A. Infantes-Molina, *Materials*. **11**, 890–907 (2018)
16. T.E.R. Fiuza, D.S. Gonçalves, I.F. Gomes, D. Zanchet, *Catal. Today* **381**, 171–180 (2020)
17. P. Li, L. Liu, W. An, H. Wang, H. Guo, Y. Liang, W. Cui, *Appl. Catal. B* **266**, 118618–118632 (2020)
18. N.S.K. Gowthaman, S. Shankar, S. Abraham John, *J. Electroanal. Chem.* **812**, 37–44 (2018)
19. W. Xu, J. Jia, T. Wang, C. Li, B. He, J. Zong, Y. Wang, H.J. Fan, H. Xu, Y. Feng, H. Chen, *Angew. Chem. Int. Ed.* **59**, 22246–22251 (2020)
20. M. Tominaga, Y. Taema, I. Taniguchi, *J. Electroanal. Chem.* **624**, 1–8 (2008)
21. D. Kim, C. Xie, N. Becknell, Y. Yu, M. Karamad, K. Chan, P. Yang, *J. Am. Chem. Soc.* **139**, 8329–8336 (2017)
22. D. Choeyk, A. Proszynski, G. Gladyszewski, *J. Nanosci. Nanotechnol.* **12**, 8647–8650 (2012)
23. K.U. Joshi, D. Kabiraj, A.M. Narsale, D.K. Avasthi, T.K. Gundurao, T.N. Warang, D.C. Kothari, *Surf. Coat. Technol.* **203**, 2497–2500 (2009)
24. K. Bergum, H.N. Riise, S. Gorantla, P.F. Lindberg, I.J.T. Jensen, A.E. Gunnæs, A. Galeckas, S. Diplas, B.G. Svenssak, E. Monakhov, *J. Phys.: Condens. Matter* **30**, 075702–075724 (2018)
25. K. Kumar, P. Swaminathan, *Thin Solid Films* **642**, 364–369 (2017)
26. P.L. Khoo, Y. Kikkawa, K. Satou, T. Shinagawa, M. Izaki, *Thin Solid Films* **653**, 158–164 (2018)
27. Y. Sato, S. Naya, H. Tada, *APL Mater.* **3**, 104502–114510 (2015)
28. H.Q. Huynh, K.N. Pham, B.T. Phan, C.K. Tran, H. Lee, V.Q. Dang, *J. Photochem. Photobiol., A* **399**, 112639–112676 (2020)
29. F. Amiripour, S.N. Azizi, S. Ghasemi, *Int. J. Hydrogen Energy* **44**, 605–617 (2019)
30. J. Wang, H. Zhu, D. Yu, J. Chen, J. Chen, M. Zhang, L. Wang, M. Du, *ACS Applied Mater Interfaces.* **9**, 19756–19765 (2017)
31. L. Van Turnhout, Y. Hattori, J. Meng, K. Zheng, J. Sá, *Nano Lett.* **20**, 8220–8228 (2020)
32. H. Wen, Y. Long, W. Han, W. Wu, Y. Yang, J. Ma, *Appl. Catal. A* **549**, 237–244 (2018)
33. Y. Liu, C. Xu, Y. Xie, L. Yang, Y. Ling, L. Chen, *J. Alloy. Compd.* **820**, 153440–153448 (2019)
34. D. Zeng, L. Yang, P. Zhou, D. Hu, Y. Xie, S. Li, J. Zhao, *Int. J. Hydrogen Energy* **43**, 15155–15163 (2018)
35. A. Gellé, T. Jin, L. de la Garza, G.D. Price, L.V. Besteiro, A. Moores, *Chem. Rev.* **120**, 986–1041 (2020)
36. W. Lipińska, K. Grochowska, J. Karczewski, J. Ryl, K. Siuzdak, *Chem. Eng. J.* **399**, 125673–125685 (2020)
37. J. Wawrzyniak, J. Karczewski, P. Kupracz, K. Grochowska, K. Załęski, O. Pshyk, E. Coy, M. Barmański, M. Szkoda, K. Siuzdak, *Appl. Surf. Sci.* **508**, 145143–145153 (2019)
38. W. Lipińska, K. Siuzdak, J. Ryl, P. Barski, G. Śliwiński, K. Grochowska, *Mater. Res. Express.* **6**, 1150e3 (2019)
39. K. Grochowska, K. Siuzdak, J. Karczewski, M. Szkoda, G. Śliwiński, *Plasmonics* **12**, 1939–1946 (2016)
40. K. Grochowska, K. Siuzdak, Ł. Macewicz, F. Skiba, M. Szkoda, J. Karczewski, G. Śliwiński, *Appl. Surf. Sci.* **418**, 472–480 (2017)
41. N. Fredj, T.D. Burleigh, *J. Electrochem. Soc.* **158**, C104 (2011)
42. L. Skowronski, A.A. Wachowiak, A. Grabowski, *Appl. Surf. Sci.* **388**, 731–740 (2016)
43. H.N. Umh, S. Yu, Y.H. Kim, S.Y. Lee, J. Yi, *ACS Appl. Mater. Interfaces.* **8**, 15802–15808 (2016)
44. L. Guo, Q. Sun, K. Marcus, Y. Hao, J. Deng, K. Bi, Y. Yang, *J. Mater. Chem. A* **6**, 22005–22012 (2013)
45. J.C. Scaiano, K.G. Stamplecoskie, G.L. Hallett-Tapley, *Chem. Commun.* **48**, 4798–4808 (2012)
46. V.N. Nguyen, M.V. Nguyen, T.H.T. Nguyen, M.T. Doan, L.L.T. Ngoc, E. Janssens, A. Yadav, P. Lin, M.S. Nguyen, N.H. Hoang, *Catalysts* **10**, 261–272 (2020)
47. M. Lai, H. Yong, K. Zhong, W. Wang, J. Huang, S. Yao, X. Wang, *Surf. Rev. Lett.* **26**, 1950040–1950048 (2019)
48. S.B. Patel, A. Hamlekhan, D. Royhman, A. Butt, J. Yuan, T. Shokuhfar, C.G. Takoudis, *J. Mater. Chem. B* **2**, 3597–3608 (2014)
49. O. Fesenko, L. Yatsenko, *Springer Proc. Phys.* **167**, 1–489 (2015)

50. L. Qian, R. Li, L. Zhou, Y. Liu, M. Yu, F. Xiong, X. Hao, *BioResources* **10**, 4391–4402 (2015)
51. C.L. Bracey, P.R. Ellis, G.J. Hutchings, *Chem. Soc. Rev.* **38**, 2231–2243 (2009)
52. O. Rocha-Rocha, M. Cortez-Valadez, G. Calderón-Ayala, C.E. Martínez-Nuñez, M. Pedroza-Montero, M. Flores-Acosta, *Phys. Lett. A* **383**, 125985–125992 (2019)
53. Y. Deng, A.D. Handoko, Y. Du, S. Xi, B.S. Yeo, *ACS Catal.* **6**, 2473–2481 (2016)
54. T. Kalaivani, P. Anilkumar, *SILICON* **10**, 1679–1686 (2018)
55. A.A. Mosquera, J.M. Albella, V. Navarro, D. Bhattacharyya, J.L. Endrino, *Sci. Rep.* **6**, 32171–32184 (2016)
56. W. Lipińska, J. Ryl, P. Slepiski, K. Siuzdak, K. Grochowska, *Measurement* **174**, 109015 (2021)
57. W. Zhan, J. Wang, H. Wang, J. Zhang, X. Liu, P. Zhang, H. Zhu, *J. Am. Chem. Soc.* **139**, 8846–8854 (2017)
58. H. Park, S.E. Kim, *IEEE Trans. Components Packag. Manuf. Technol.* **1**, 332–338 (2019)
59. A. Bohme, F. Sterl, E. Kath, M. Ubl, V. Manninen, H. Giessen, *ACS Photonics* **6**, 1863–1868 (2019)
60. N. Shen, H. Xu, W. Zhao, Y. Zhao, X. Zhang, *Sensors* **19**, 1203–1213 (2019)
61. B. Sundqvist, V.K. Tolpygo, *J. Phys. Chem. Solids* **122**, 41–50 (2018)
62. W. Tan, T. Gao, Y. Wang, *Langmuir* **36**, 3836–3842 (2020)
63. M. Salari, S.H. Aboutalebi, A.T. Chidembo, I.P. Nevirkovets, K. Konstantinov, H.K. Liu, *Phys. Chem. Chem. Phys.* **14**, 4770–4779 (2012)
64. J. Li, N. Yu, H. Jiang, J. Leng, H. Geng, *Corros. Sci.* **91**, 95–100 (2015)
65. T. Tachikawa, A. Beniya, K. Shigetoh, S. Higashi, *Catal. Lett.* **150**, 1976–1984 (2020)
66. X. Gong, Y. Gu, F. Zhang, Z. Liu, Y. Li, G. Chen, B. Wang, *Front. Mater.* **6**, 1–9 (2019)
67. P. Basnet, E.C. Anderson, Y. Zhao, *ACS Appl. Nano Mater.* **2**, 2446–2455 (2019)
68. L. Luo, T. Zhang, X. Zhang, R. Yun, Y. Lin, B. Zhang, X. Xiang, *Catalysts* **10**, 539–557 (2020)
69. M. Szkoda, A. Lisowska-Oleksiak, K. Siuzdak, *J. Solid State Electrochem.* **20**, 1765–1774 (2016)
70. G.Y. Yao, Z.Y. Zhao, *J. Mater. Chem. C* **8**, 8567–8578 (2020)
71. W. Lipińska, K. Grochowska, J. Ryl, J. Karczewski, K. Siuzdak, *ACS Appl. Mater. Interface.* **13**, 52967–52977 (2021)

Publisher's Note Springer Nature remains neutral with regard to jurisdictional claims in published maps and institutional affiliations.